A General Model for Multiphase Texture Segmentation and Its Applications to Retinal Image Analysis

Yalin Zheng*

Department of Eye and Vision Science, University of Liverpool, Liverpool, United Kingdom

Ke Chen*

Center for Mathematical Imaging Techniques and Department of Mathematical Sciences, University of Liverpool, Liverpool, United Kingdom

Abstract

In this paper we propose a general variational segmentation model for multiphase texture segmentation based on fuzzy region competition principle. An important strength of the proposed framework is that different region terms (e.g. mutual information [1], local histogram [2] models for texture-based segmentation, and piecewise constant intensity model [3] for intensity-based segmentation) can be included as appropriate to the problem. Constraints of different phases are considered by introducing Lagrangian multipliers into the energy functional, and a fast numerical solution is achieved by employing the fast dual projection algorithm [4]. The proposed model has been applied to synthetic and natural images in order to make comparisons with other competing models in literature. Our results demonstrate superiority in dealing with multiphase texture segmentation problems. To demonstrate its usefulness in biomedical applications we have applied the new model to two retinal image segmentation problems: segmentation of capillary non-perfusion regions in fluorescein angiogram and segmentation of cellular layers of the retina in optical coherence tomography, and evaluated against the gold standard set by experts. The generalized overlap analysis shows good agreement for both applications. As a generic segmentation technique our new model has the potential to be extended for wider applications.

Keywords: multiphase segmentation, texture, active contour, level set, fluorescein angiography, optical coherence tomography

1. Introduction

Image segmentation, particularly in the field of medical image segmentation, is a fundamental and challenging problem in image processing and often a vital step for high level analysis. The aim of image segmentation is to divide an image into different categories based on features, such as intensity, color or texture, where each pixel in the image should belong to one class and only one class. Segmentation of texture images is intrinsically more challenging than intensity-based ones. For texture images, detecting edges directly is problematic as it may treat intrinsic texture patterns as edges resulting unsatisfactory segmentation. Depending on the number of categories of regions to be segmented, image segmentation can be two-phase (two categories) or multiphase (more than two categories).

*Corresponding author. Department of Eye and Vision Science, University of Liverpool, Daulby Street, Liverpool, L69 3GA, United Kingdom. Telephone: +44 (0)151 706 4083. Fax: +44 (0)151 706 5802.

Email addresses: yalin.zheng@liv.ac.uk (Yalin Zheng), k.chen@liv.ac.uk (Ke Chen)

URL: http://pcwww.liv.ac.uk/~yzheng/ (Yalin Zheng), www.liv.ac.uk/~cmchenke/ (Ke Chen)

Multiphase segmentation is extremely valuable for medical image analysis as in many applications the structure of interest often is often surrounded by other structures or organs.

In this paper we will limit our discussion to energy minimization models and more specifically region-based active contour models. These models can be modeled mathematically and optimized using efficient solvers (e.g. graph cut [5], multigrid [6], dual projection algorithm [4], convexification method [7]). More importantly, they have thrived for their robustness and flexibility in dealing with different applications [8, 3, 1, 9, 2]. For two-phase segmentation a plethora of models have been proposed primarily for intensity-based segmentation (e.g. piecewise constant intensity model [3] and few for texture segmentation models [8, 1, 2]. Considerable effort has also been made to formulate a general framework to unify all the two-phase segmentation models [10, 11, 12]. In particular the concept of fuzzy region competition [12] has inspired recent total variational (TV) multiphase segmentation models [13, 14] and the proposed model in this paper.

For multiphase intensity-based segmentation, hierarchical implementation has been proposed for piecewise constant image [15, 6, 16], and also for piecewise smoothing image [17]. The most common strategy for multiphase intensity-based segmentation is to tackle the problem by generalizing the existing two-phase models with more level set functions [18, 19, 20, 21, 22, 23]. Multiphase texture segmentation is understudied and limited number of models are available including hierarchical implementation strategy [24], feature-based models [25, 26], and the recent total variational models [13, 14]. The TV multiphase segmentation models require a predefined stopping criteria requested by the hierarchical strategy [24], and the need of appropriate feature filters and also optimal filter parameters [25, 26]), as such there is a real interest to go for further investigations with TV multiphase segmentation models.

In this paper we will propose a general variational segmentation model for multiphase texture / intensity segmentation. In order to demonstrate the usefulness of the proposed framework we will apply our new models to two challenging retinal image segmentation problems which represent two-phase and multiphase problems respectively. A wide range of imaging techniques have been used in the management of retinal disease and automated analysis of retinal images is an active area [27]. We first consider the segmentation problem of capillary non-perfusion (CNP) regions in fluorescein angiography (FA) image of the retina which is relevant to retinal ischemic diseases including vein occlusion, ischaemic diabetic retinopathy (DR), malarial retinopathy (MR) and so on. The second application is on automated segmentation of the retina layers in optical coherence tomography (OCT) images. OCT is an optical analogue of ultrasound imaging and is capable of resolving the individual retinal layers and enable researchers to look for links between individual retinal layers and their clinical relevance [28, 29].

The main contributions of this paper are: 1) a general segmentation framework that unifies a wide range of texture or non-texture segmentation models; 2) a fast solver to solve the proposed model; 3) introduction of Lagrangian multipliers allowing that powerful parallel computing techniques can be used to speed up the segmentation process implying its great potential for solving real applications; and 4) applications to two retinal image segmentation problems with good performance demonstrating the importance of texture segmentation in real-world problems.

The remainder of this paper is organized as follows. In Section 2 we briefly review some related segmentation models, and propose a novel segmentation model and provide a stable and efficient minimization strategy for it. In Section 3 we first present some experimental results on synthetic and photographic images with comparison to previous models, and apply the new models to two real

segmentation problems and presented results of objective evaluation. We conclude our paper in Section 4.

2. Models

Let Ω be a bounded open subset of R^d when $d = 2$ is for two-dimensional (2D) images and 3 for three dimensional (3D) images respectively. Let $I : \Omega \to R$ be the given grayscale image. The aim of multiphase segmentation is to partition Ω into N regions Ω_i, $1 \leq i \leq N$ where $\Omega_i \bigcap \Omega_j = 0, i \neq j$ and $\sum_{i=1}^{N} \Omega_i = \Omega$. $\partial\Omega_i$ is the boundary for region Ω_i and we have $\partial\Omega = \bigcup_{i=1}^{N} \partial\Omega_i$. The general framework for multiphase segmentation can be described as follows.

$$E(U, R) = \sum_{i=1}^{N} \int_{\Omega} g|\nabla u_i| dx + \sum_{i=1}^{N} \lambda \int_{\Omega} u_i r_i(I, u_i) dx, \quad (1)$$

subject to

$$\text{(i)} \quad \sum_{i=1}^{N} u_i = 1, \quad \text{(ii)} \quad 0 \leq u_i \leq 1, i = 1, \cdots, N. \quad (2)$$

$U = (u_1, \cdots, u_N)$ and $R = (r_1, \cdots, r_N)$ are the membership functions and region terms respectively. $\int_{\Omega} g|\nabla u_i| dx$ is the weighted TV norm: g can be the edge map [30] or 1 by default for standard TV norm. The first term of the energy functional is the length of boundaries and the second term is the region term. It is the use of different region terms that affects the behavior of this model. If there is no nonlinear relations between different r_is (e.g. [31]), multiphase segmentation can be achieved by minimizing the above energy functional. This formulation will be of some help for a performance comparison with other method of the same kind.

2.1. Two-phase Models

Classical two-phase models are the special case of (1) where $N = 2$. For the Chan and Vese (CV) model [3], the regions terms can be given as follows.

$$r_i = (c_i - I(x))^2, \quad (3)$$

where $c_i, i = 1, 2$ are the mean intensity values in Ω_1 and Ω_2 respectively.

For the region competition model [8] and mutual information model [1], the region term can be given

$$r_i = -\log(P_i|\alpha_i), \quad (4)$$

The main difference between the model [8] and the model [1] is in the way probability density function (PDF) is modeled for the inner and outer regions $P_i, i = 1, 2$ respectively. The first model [8] assumes that the PDFs are Gaussian distributions while the later one [1] non-parametrically estimates the PDFs using the well-know Parzen window approach (for details please refer to [32]). As such the second model [1] allows more flexibility to deal with a more wide range of segmentation problems. The mutual information idea is also used by Herbulot et al. for moving video object segmentation [33].

One of the most recent local histogram models can achieve global convex minimization and thus global optimal solution [2]. The related region terms can be defined as

$$r_i = W_1(P_i, P_x), \quad (5)$$

where W_1 is the Wasserstein distance with exponent 1. P_i is the constant histogram to approximate and P_x is the local histograms in region Ω_i. Notably, the Wasserstein distance has been further generalized to arbitrary dimension and used in a more recent active contour model [34].

2.2. Multiphase Texture Segmentation Models

Li et al. proposed a multiphase texture segmentation model using mutual information [13]. By relaxing $u_N = 1 - \sum_{i=1}^{N-1} u_i$, the energy (1) is approximated by

$$E(U, P) = \sum_{i=1}^{N-1} \left(\int_{\Omega} |\nabla u_i| dx - \lambda \int_{\Omega} u_i \log(\frac{P_N(I, u_N)}{P_i(I, u_i)}) dx \right). \quad (6)$$

This model is sensitive to initialization of membership functions for $N \geq 3$ problems. The strategy of relaxing

the constraint $u_N = 1 - \sum_{i=1}^{N-1} u_i$ makes the Nth phase dependent on the other phases, which makes further generalization difficult. We remark that another model by Choy et al. [14] uses hybrid region terms that combine spatial and frequency information of regions, which may also be studied in our proposed framework.

2.3. The Proposed Multiphase Segmentation Model

From our observations both the above multiphase texture segmentation models [13, 14] have merely considered the mutual information based region term. Therefore our first contribution of this paper is to advocate a model that can generalize all the multiphase texture segmentation models as well as intensity ones by embracing the full strength of the concept of fuzzy region competition (Note, no previous effort has been made to generalize the local histogram strategy [2] for multiphase segmentation yet). Since the computational cost is usually high for multiphase segmentation problem, therefore our second contribution is to propose an efficient solver for the unifying model which enables high performance computing for real-time applications in the future.

Following the principle of Euler-Lagrangian optimization, by treating the constraint $\sum_{i=1}^{N} u_i = 1$ explicitly, our general variational model minimizes the following energy functional

$$E(U,R) = \sum_{i=1}^{N} \left(\int_\Omega g|\nabla u_i| dx + \frac{1}{2\gamma} \int_\Omega (1 - \sum_{i=1}^{N} u_i)^2 dx - \lambda \int_\Omega u_i r_i(I, u_i) dx \right). \tag{7}$$

Clearly comparing to previous work (6), our unifying model allows a change of fidelity term r_i from different models and permits the direct regularization of membership functions for all N phases. The added regularization will provide increased robustness in multiphase segmentation.

As mentioned, the above energy will lead to challenging nonlinear equations to solve. Here we propose a practical solution strategy. We first approximate the minimizing functional in (7) by introducing auxiliary variables. More specifically, auxiliary membership variables $V = (v_1, \cdots, v_N)$ are added to (7), and now $E(U,R)$ will be formulated as

$$E(U,V,R) = \sum_{i=1}^{N} \left(\int_\Omega g|\nabla u_i| dx + \frac{1}{2\gamma} \int_\Omega (1 - \sum_{i=1}^{N} v_i)^2 dx + \frac{1}{2\theta} \int_\Omega (u_i - v_i)^2 dx + \lambda \int_\Omega v_i r_i(I, u_i) dx \right). \tag{8}$$

Here the convex form $\int_\Omega (u_i - v_i)^2 dx$ is to force u and v close to each other, and $\theta > 0$ is a small parameter. Alternating minimization of (8) against U, V, and R lead to tractable solution methods. More specifically, While keeping R fixed, U and V in (8) can be solved by the following alternating optimization procedure.

Step 1. First, we consider the energy minimization problem below to solve U with fixed R and V.

$$E_1(U,V,R) = \sum_{i=1}^{N} \left(\int_\Omega g|\nabla u_i| dx + \frac{1}{2\theta} \int_\Omega (u_i - v_i)^2 dx \right). \tag{9}$$

This energy is tractable under Chambolle's fast projection algorithm [4] as follows,

$$u_i(x) = v_i(x) - \theta div p_i(x). \tag{10}$$

Here p_i can be solved by a fixed point method by initializing $p_i^0 = 0$,

$$p_i^{n+1} = \frac{p_i^n + dt\nabla(div p_i^n - v_i/\theta)}{1 + \frac{dt}{g}|div p_i^n - v_i/\theta|}, \tag{11}$$

where $dt \leq 1/8$ is the time step. See [4] for more details.

Step 2. Second, we solve V with fixed U and R by considering the energy minimization problem below

$$E_2(U,V,R) = \sum_{i=1}^{N} \left(\frac{1}{2\gamma} \int_\Omega (1 - \sum_{i=1}^{N} v_i)^2 dx + \frac{1}{2\theta} \int_\Omega (u_i - v_i)^2 dx - \lambda \int_\Omega v_i r_i dx \right). \tag{12}$$

For fixed R and U, the quantity V can be directly derived by solving a system of linear equations. For simplicity the

solution is given as follows,

$$\widetilde{v_i} = u_i - \lambda\theta r_i - \frac{\theta}{\gamma + N\theta}\left(\sum_{j=1}^{N}(u_j - \lambda\theta r_j) - 1\right), \quad (13)$$

$$v_i = \max\left\{\min\left\{\widetilde{v_i}, 1\right\}, 0\right\}. \quad (14)$$

2.4. The Overall Algorithm

Our algorithm can be summarized in the following steps:

- Initialization: Initialize u_i and v_i.
- Iteration
  - Update r_i, where r_i can be in any form (e.g., (3), (4), (5) or any other);
  - Update v_i by (13);
  - Update u_i by (10);
  - Terminate when $\| U_{new} - U_{old} \| \leq \epsilon$.

Here $\| \cdot \|$ denotes the Euclidean distance and ϵ is a small positive number.

Compared to the two previous models [13] [14], the most important strength of the proposed model is its generality and flexibility for dealing with different segmentation tasks. This is achieved by employing different types of region term r_i (e.g. (4), (5), (3)) as appropriate. For further flexibility the first term in (1) can also be replaced by other geometric scale measures.

3. Experimental Results

In this section we first perform proof-of-concept experiments on our models and compare them with other existing ones on synthetic and natural images. Then we apply our models to two real medical imaging applications and evaluate against gold standard set by expert manual segmentation. For simplicity, we denote the tested methods respectively by

- M1 — Two-phase mutual information model [1]
- M2 — Two-phase local histogram model [2]
- M3 — Two-phase CV model [3]
- M4 — Li's multiphase model [13]
- M5I — Our model with r_i defined in (4)
- M5II — Our model with r_i defined in (5)
- M5III — Our model with r_i defined in (3)

We implement the M1, M2 and M3 by the fast dual projection solvers rather than the original ones for computational efficiency. We only test them for two-phase segmentation problems for which they are initially designed. In all the experiments, some parameters are fixed as follows: $g = 1$, $\theta = 0.01$, $\gamma = 0.001$, $dt = 1/8$ and error tolerance $\epsilon = 1e-4$, maximum iteration number of $10,000$. λ is tuned towards the best possible results. Similarly, when the M2 and M5II are used, the window size (W) for computing the local histogram is experimentally chosen to handle different types of images. In general, when the texture scale is large, a large window size is preferred and vice versa. Different grayscale levels are used to show the segmentation results.

3.1. Proof-of-concept Experiments

We first demonstrate that the proposed framework works as expected, see Fig. 1 for illustration. In Fig. 1(a), we test a synthetic noisy image as used in [13] where the distributions for the foreground and the background are Gaussian with different means and the same variance. Fig 1(i) contains an images of natural scene. The task here is to segment the zebra as the foreground. The intensity-based models (M3 and M5III) only segment the strips of the zebra's body rather than the whole zebra. This experiment demonstrates that intensity-based models such as the M3 and M5III cannot handle texture segmentation problem while all the texture-based approaches have successfully segment the zebra as expected.

In the second set of tests, we first test our proposed framework (M5I, M5II and M5III) and M4 on two three-phase texture segmentation problems, as shown in Fig. 2(a)

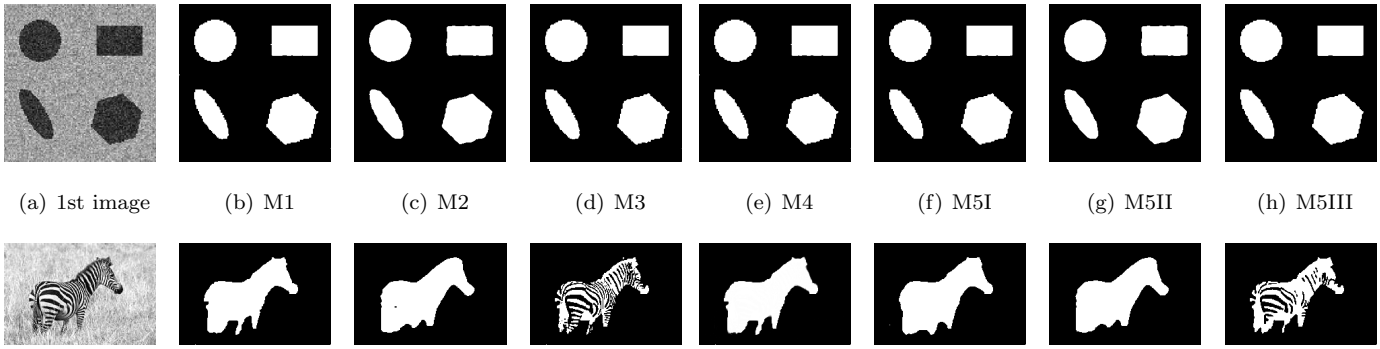

(a) 1st image (b) M1 (c) M2 (d) M3 (e) M4 (f) M5I (g) M5II (h) M5III

(i) 2nd image (j) M1 (k) M2 (l) M3 (m) M4 (n) M5I (o) M5II (p) M5III

Figure 1: Experimental results on two-phase segmentation for synthetic and natural scene images. $\lambda = 0.3$ for all the experiments except for M3 and M5III ($\lambda = 10$). Window size is 3 and 7 for the 1st and 2nd images respectively.

and 2(f), The M5I and M5II yield satisfactory performance as expected while with the same initialization the M4 failed for the first case (Fig. 2(b)). It is not surprising that the M5III in general cannot handle textures well. We also apply our segmentation models to a composite image comprising five different textures from the Brodatz database as is shown in Fig. 2(k), and our results are pleasing for the M5I and M5II as shown in Fig. 2(m) and 2(j). Again, the intensity-based model M5III fails to segment the image correctly. The M4 also fails as the image is segmented into four phases but not five. This might due to its sensitivity to initialization as noted by the authors in [13]. It is worth mentioning that for all the above experiments, we only showed the original images and the results of different segmentation methods for side-by-side comparison: visual inspection of the segmentation results is still the most simple and intuitive way for comparison especially when there is no reference standard available.

3.2. Two Retinal Image Applications

In this subsection, we apply our new models to two retinal image segmentation problems which represent two-phase and multiphase problems respectively. Objective evaluation is a vital step in algorithmic development and applications, and here we evaluate their performance against the practical gold standard obtained from expert manual delineations. For the readers' interest, we will begin with introducing the validation criteria, followed by presentation of the segmentation problems and our evaluation results.

In this work, the generalized Dice coefficient (GDC) [35] is used for the purpose of validation (Matlab program is implemented following the original paper). The GDC can be defined as follows

$$GDC = \frac{\sum_k \beta_k \sum_l \alpha_l \sum_i 2MIN(A_{kli}, B_{kli})}{\sum_k \beta_k \sum_l \alpha_l \sum_i (MAX(A_{kli}, B_{kli}) + MIN(A_{kli}, B_{kli}))}. \quad (15)$$

In (15), i is the pixel index in the images, l represents the label index and k denotes image pairs. A_{kli} and B_{kli} represent pixel label values in a pair of segmentation images having values in the range $[0, 1]$. The $MIN()$ and $MAX()$ operators are the intersection and union of fuzzy sets respectively. The parameter α_l affects the relative weighting of different labels. With $\alpha_l = 1$, labels with larger volumes $\overline{V_l}$ (areas) contribute most of the overlap. In the case $\alpha_l = 1/\overline{V_l}$, it will make the relative weighting of different labels equal. If $\alpha_l = (1/\overline{V_l})^2$ it gives labels of smaller volume higher weighting. β_k is the relative weights for different images and is set to 1 by default. The GDC is an overall measure of consistency over multiple labels on all the images under consideration. For $k = 1$ and $l = 1$, the GDC becomes the standard Dice coefficient. GDC ranges from 0 (no agreement) to 1 (perfect agreement). It is generally accepted that a GDC value higher

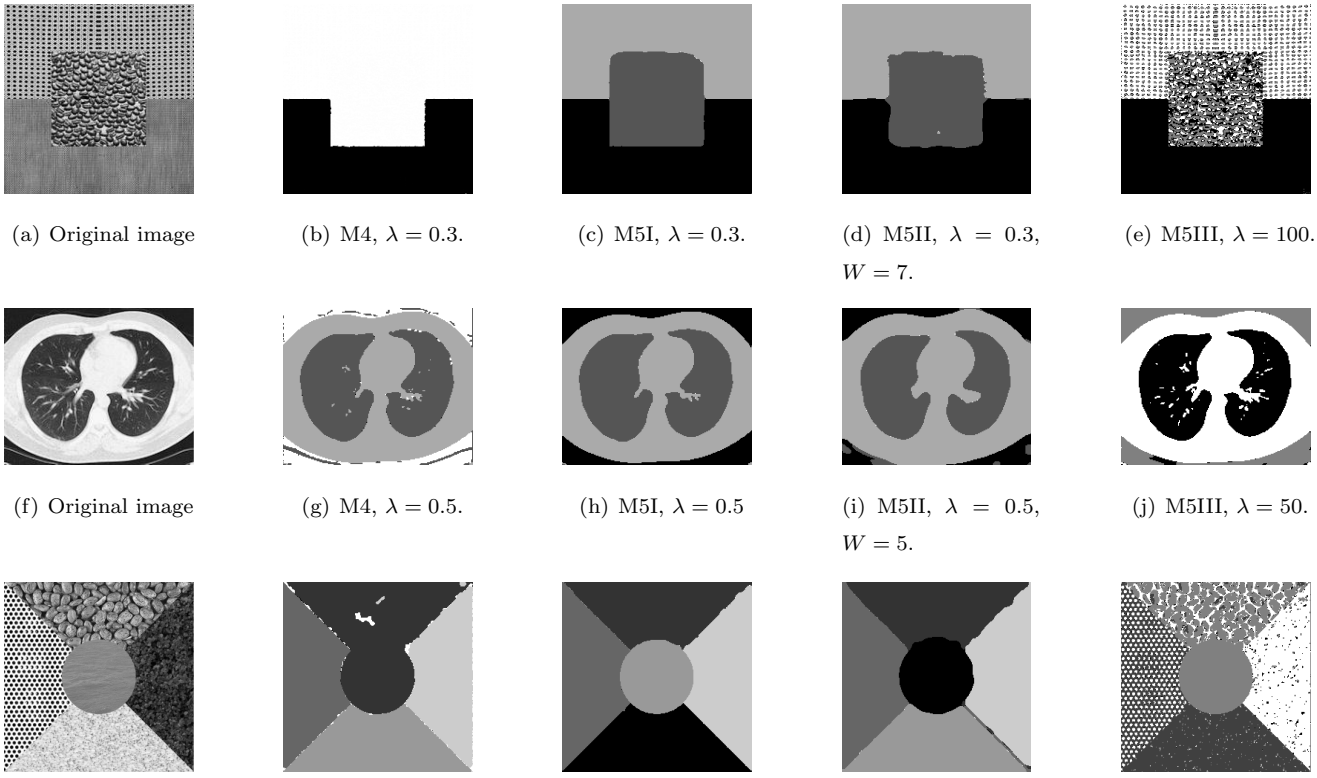

(a) Original image (b) M4, $\lambda = 0.3$. (c) M5I, $\lambda = 0.3$. (d) M5II, $\lambda = 0.3$, $W = 7$. (e) M5III, $\lambda = 100$.

(f) Original image (g) M4, $\lambda = 0.5$. (h) M5I, $\lambda = 0.5$ (i) M5II, $\lambda = 0.5$, $W = 5$. (j) M5III, $\lambda = 50$.

(k) Original image (l) M4, $\lambda = 0.3$. (m) M5I, $\lambda = 0.3$. (n) M5II, $\lambda = 0.1$, $W = 7$. (o) M5III, $\lambda = 100$

Figure 2: Experimental results of multiphase segmentation.

than 0.70 indicates excellent agreement when considering performance of segmentation techniques [36].

3.2.1. Segmentation of Capillary Non-perfusion Regions

Our first application is automated segmentation of capillary non-perfusion regions in FA images. The retina demand extremely high energy and nutrients and in particular its sensory cells (photoreceptors) have the highest metabolic rate amongst all cells of the body. A sufficient blood supply is essential to provide it a good delivery of nutrients and elimination of waste products. Retinal vessel structure can be compromised due to the pathogenesis of a wide spectrum of retinal ischemic diseases and CNP is a hallmark common to all of the aforementioned diseases. CNP can be best detected using FA images [37], where a series of images of the retina are taken after injection of a fluorescent dye into the arm of the patient. FA remains the standard diagnostic imaging technique for visualizing the retinal vasculature and in making treatment and management decisions. The assessment of FA remains a subjective process and also extremely difficult for untrained eyes to spot these traits. Therefore it is highly desirable to design an algorithm that can assist quantitative analysis of FA images in an automated manner. So far only few previous work concerning CNP detection has been published in the literature [38, 39]. Due to loss of capillaries, the CNP regions have a relatively dull appearance, see Fig. 3(a) for MR and 3(k) for DR, which indicates that texture strategy is appropriate for consideration.

In this experiment 25 sub-images are obtained with a size of 256 by 256 pixels. Boundaries of all the CNP regions within them are delineated manually by a retinal specialist for the purpose of evaluation, as shown in the second column in Fig. 3. Here we apply all the three strategies (M5I, M5II and M5III) and the results are shown

in the third, fourth and fifth column of Fig 3.

Of three methods, the M5II yields the best GDC value (0.609) followed by M5I (0.604) showing they have similar good performance. On the other hand, the M5III only has a relatively fair agreement (0.493) and actually failed to distinguish the CNPs from non-CNPs in most cases. Further statistical analysis is also performed on the Dice coefficient of each image (special case of GDC when $k = 1$ and $l = 1$) and the result shows that there was a statistically significant difference between groups as determined by one-way analysis of variance (ANOVA) ($F(2, 72) = 6.127$, $p = 0.003$). A Tukey post-hoc test revealed that the Dice coefficient value is statistically significantly higher by using the M5I (0.590 ± 0.142, $p = 0.018$) and M5II (0.608 ± 0.123, $p = 0.123$) compared to the M5III (0.474 ± 0.172, $p = 0.005$). There were no statistically significant differences between the M5I and M5II ($p = 0.906$).This experiment proves the strength of texture segmentation models, and only these models (M5I and M5II) will be further evaluated in the subsequent experiment.

It is worth mentioning that during discussion with clinicians that they feel it is very challenging to delineate all the CNP boundaries because of the variations in size, contrast and appearance of other pathologies. In this study, manual delineation has been used as a gold standard, which may be sub-optimal. It is important to establish and evaluated the reproducibility and repeatability of manual delineations in the future. On the other hand, inconsistency of manual grading of CNP is one of the motivations for automated segmentation.

3.2.2. Segmentation of Retinal Layers in OCT

In our second application we will consider automated segmentation of the main retinal layers in OCT images, as shown in in the first column of Fig. 4. OCT is an indispensable tool for diagnosis and management of ocular diseases and in particular retinal diseases, including DR, age-related macular degeneration and glaucoma (three leading causes of vision loss worldwide). Automated detection and quantitative analysis of retinal layers is an important challenge due to their significance in the management of eye disease. Although a number of intensity-based segmentation approaches have previously be described, such as graph approach [27], heuristic approach based on gradient information [40], active contour [41], automated retinal layer segmentation remains an open problem principally due to challenges within the image including for example inherent speckle noise, intensity inhomogeneity within different layers, and disturbance of layers complicated by pathology.

We will only consider segmentation of the main retinal layers in the foveal area of the retina. The fovea is the center of the retina and provides us with the essential sharp vision and color vision. Three major layer structures can be seen all the time in this area. From the innermost layer to the outermost are: (i) the inner retina; (ii) the outer retina, and (iii) the retinal pigment epithelium (RPE)/Bruch's complex. The first band looks relatively bright (hyper-reflective), but less than the third band. The second band has similar view of the area immediately next to the RPE/Bruch's complex corresponding to the choroid. The dark (hypo-reflective) area on the top corresponding to the vitreous and the area at the bottom have the similar appearance of low intensity. This parallel anatomical arrangement suggests that a three-phase segmentation model is sufficient to address this problem with the help of simple region operations afterwards. Note, the other structures such as the vitreous and the choroid have also been obtained, which could be further explored for their value in management of disease.

A total of 18 OCT images of the fovea region are collected from OCT scans acquired on a Spectralis HRA+OCT device (Heidelberg Engineering, Heidelberg, Germany). Each image has a size of 256 by 128 pixels and the boundaries of three layers are delineated manually by a clinical expert

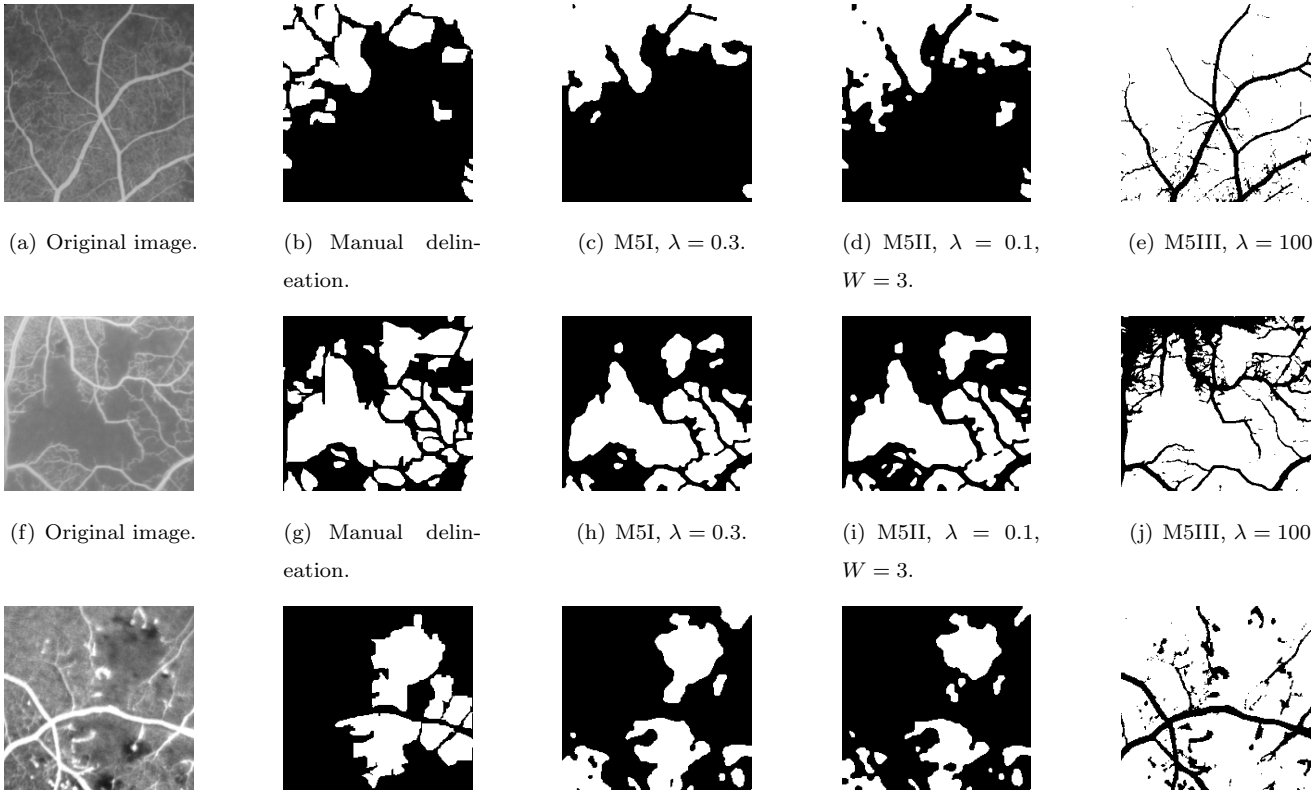

(a) Original image. (b) Manual delineation. (c) M5I, $\lambda = 0.3$. (d) M5II, $\lambda = 0.1$, $W = 3$. (e) M5III, $\lambda = 100$

(f) Original image. (g) Manual delineation. (h) M5I, $\lambda = 0.3$. (i) M5II, $\lambda = 0.1$, $W = 3$. (j) M5III, $\lambda = 100$

(k) Original image. (l) Manual delineation. (m) M5I, $\lambda = 0.3$. (n) M5II, $\lambda = 0.1$, $W = 3$. (o) M5III, $\lambda = 100$

Figure 3: Experimental results of CNP segmentation.

Table 1: Agreement between the program and manual delineation. $\overline{V_l}$ is the average size of two measures of label l.

	M5I			M5II		
Weight	1	$1/\overline{V_l}$	$(1/\overline{V_l})^2$	1	$1/\overline{V_l}$	$(1/\overline{V_l})^2$
GDC	0.783	0.775	0.766	0.787	0.780	0.774

as gold standard. Labels of each layer are generated from their delineations and shown in the images of the second column of Fig. 4. We apply the M5I and M5II models to all the images and our experiments have yielded convincing results. Excellent agreement is observed for both strategies (GDC values over 0.75 for all three weighting schemes), as shown in Table 1. The M5II again gives slightly better results than the M5I, but not statistically significant (Mann-Whitney U test, $p > 0.05$).

4. Conclusions

Multiphase texture segmentation problem presents a significant challenge in the field of image segmentation. In this paper we have proposed a unifying model for multiphase texture segmentation by generalizing the concept of fuzzy region competition. As such our new model provides the flexibility of using different region terms to guide the segmentation as required by specific segmentation criteria. Constraints of the membership functions are elegantly handled by Lagrangian multipliers in our energy minimization functional. The functional is solved by a fast global minimization strategy. The mutual information based and local histogram based strategies have been used to demonstrate texture segmentation while the CV region term has been used to demonstrate its capability to be generalized for other applications. Other strategies such as smooth intensity models can also be readily included in the future.

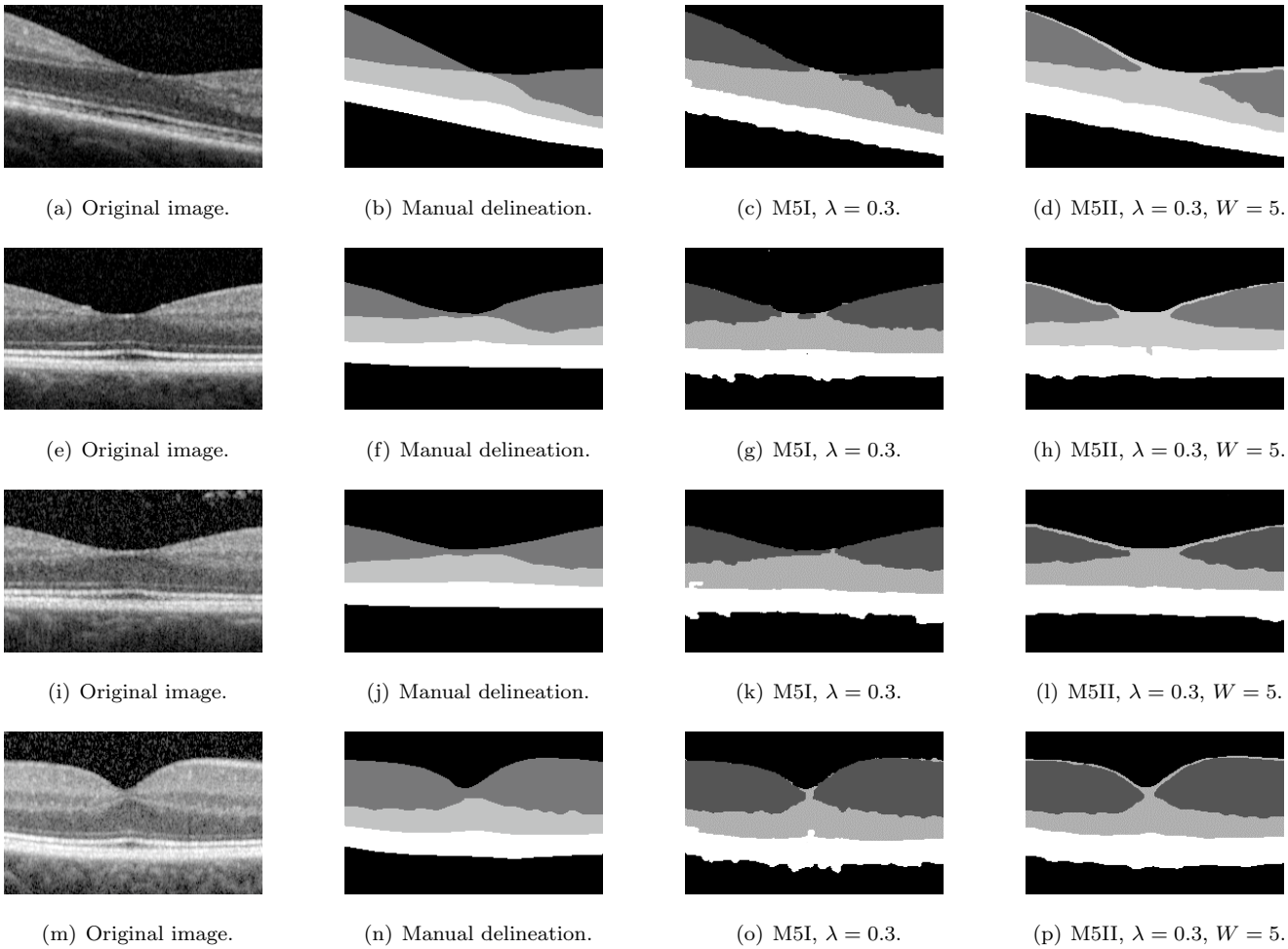

(a) Original image. (b) Manual delineation. (c) M5I, $\lambda = 0.3$. (d) M5II, $\lambda = 0.3$, $W = 5$.

(e) Original image. (f) Manual delineation. (g) M5I, $\lambda = 0.3$. (h) M5II, $\lambda = 0.3$, $W = 5$.

(i) Original image. (j) Manual delineation. (k) M5I, $\lambda = 0.3$. (l) M5II, $\lambda = 0.3$, $W = 5$.

(m) Original image. (n) Manual delineation. (o) M5I, $\lambda = 0.3$. (p) M5II, $\lambda = 0.3$, $W = 5$.

Figure 4: Experimental results of OCT segmentation.

An advantage of our model is that it explicitly determines all the regions during the optimization process, such that advanced computing techniques such as parallel computing can be introduced to speed up the process.

Our application to the synthetic and natural imaging data have demonstrated comparable, if not better, results when compared to the previous models. We have also applied the proposed models to two challenging segmentation problems encountered in retinal image applications to demonstrate the strength of texture segmentation in tackling real-world problem. For both applications the generalized overlap measure analysis has demonstrated good agreements between the results from our approach and the manual segmentations. Our experimental results have showed that the M5II performed slightly better than M5I but the difference is not statistically significant. For the CNP segmentation we are considering to apply our new models to a large dataset and to explore its potential as a powerful tool in management of ischemic retinal diseases. For the retinal layer segmentation in OCT images, so far we only considered segmentation of the three major bands of the retina which are always observable in the fovea region, as is shown in Fig. 4(m) and 4(i). The current work can provide us with a good starting point to explore segmentation of all the retinal layers. We also plan to extend our work to 3D segmentation to address the challenge in volumetric data analysis.

One of the challenges of the segmentation using iterative strategy is the computational cost. So far our program has not been optimized for speed and this is part of the

reasons we only considered images with relatively small size for both real applications. We envisage that further optimization can be achieved by hardware such as graphic processing unit (GPU) or software techniques in the future.

In summary, we have proposed a unifying segmentation model enabling multiphase segmentation and our experimental results from two retinal image segmentation applications have demonstrated its readiness for real world applications. It is expected as a generic multiphase segmentation tool it will find wider applications.

Acknowledgment

Dr Yalin Zheng thanks the Foundation for the Prevention of Blindness that provided financial support for his research. The authors also thank Dr William R. Crum of the Department of Neuroimaging, Institute of Psychiatry, King's College London, for providing advices on computing the general overlapping coefficient.

[1] J. M. Kim, J. W. Fisher, A. Yezzi, M. Cetin, A. S. Willsky, A nonparametric statistical method for image segmentation using information theory and curve evolution, IEEE Trans Image Process 14 (2005) 1486–1502.

[2] K. Ni, X. Bresson, T. F. Chan, S. Esedoglu, Local histogram based segmentation using the Wasserstein distance, Int J Comput Vis 84 (2009) 97–111.

[3] T. F. Chan, L. A. Vese, Active contours without edges, IEEE Trans Image Process 10 (2001) 266–277.

[4] A. Chambolle, An algorithm for total variation minimization and applications, J Math Imaging Vis 20 (2004) 89–97.

[5] T. P. Gurholt, X. C. Tai, 3D multiphase piecewise constant level set method based on graph cut minimization, Numer Math Theor Meth Appl 2 (2009) 403–420.

[6] N. Badshah, K. Chen, On two multigrid algorithms for modeling variational multiphase image segmentation, IEEE Trans Image Process 18 (2009) 1097–1106.

[7] R. Yildizoglu, J.-F. Aujol, N. Papadakis, Active Contours without Level Sets, in: Proc IEEE ICIP-2012, 2012, pp. 1–4.

[8] S. C. Zhu, A. Yuille, Region competition: Unifying snakes, region growing, and Bayes/MDL for multiband image segmentation, IEEE Trans Pattern Anal Mach Intell 18 (1996) 884–900.

[9] F. Lecellier, S. Jehan-Besson, J. Fadili, G. Aubert, M. Revenu, E. Saloux, Region-based active contour with noise and shape priors, in: Proc IEEE ICIP-2006, 2006, pp. 1649–1652.

[10] G. Aubert, M. Barlaud, O. Faugeras, S. Jehan-Besson, Image segmentation using active contours: Calculus of variations or shape gradients?, SIAM J. Appl. Math. 63 (2003) 2128–2154.

[11] S. Jehan-Besson, M. Barlaud, G. Aubert, Dream^{2}s: Deformable regions driven by an Eulerian accurate minimization method for image and video segmentation, Int J Comput Vision 53 (2003) 45–70.

[12] B. Mory, R. Ardon, Fuzzy region competition: A convex two-phase segmentation framework, Proc of Scale Space and Variational Methods in Computer Vision 4485 (2007) 214–226.

[13] F. Li, M. K. Ng, Kernel density estimation based multiphase fuzzy region competition method for texture image segmentation, Commun Comput Phys 8 (2010) 623–6410.

[14] S.-K. Choy, M.-L. Tang, C.-S. Tong, Image segmentation using fuzzy region competition and spatial/frequency information, IEEE Trans Image Process 20 (2011) 1473–1484.

[15] M. Jeon, M. Alexander, W. Pedrycz, N. Pizzi, Unsupervised hierarchical image segmentation with level set and additive operator splitting, Pattern Recognit Lett 26 (2005) 1461–1469.

[16] K. Ni, B. W. Hong, S. Soatto, T. F. Chan, Unsupervised multiphase segmentation: A recursive approach, Comput Vis Image Underst 113 (2009) 502–510.

[17] S. Gao, T. D. Bui, Image segmentation and selective smoothing by using Mumford-Shah model, IEEE Trans Image Process 14 (2005) 1537–1549.

[18] T. F. Chan, L. A. Vese, An efficient variational multiphase motion for the Mumford-Shah segmentation model, Proc of 34th Asilomar Conf on Signals, Systems & Computers (2000) 490–494.

[19] L. A. Vese, T. F. Chan, A multiphase level set framework for image segmentation using the Mumford and Shah model, Int J Comput Vis 50 (2002) 271–293.

[20] L. Bertelli, B. Sumengen, B. S. Manjunath, F. Gibou, A variational framework for multiregion pairwise-similarity-based image segmentation, IEEE Trans Pattern Anal Mach Intell 30 (2008) 1400–1414.

[21] F. Li, M. K. Ng, T. Zeng, C. Shen, A multiphase image segmentation method based on fuzzy region competition, SIAM J Imaging Sci 3 (2010) 277–299.

[22] M. Hintermuller, A. Laurain, Multiphase image segmentation and modulation recovery based on shape and topological sensitivity, J Math Imaging Vis 35 (2009) 1–22.

[23] N. Paragios, R. Deriche, Geodesic active regions: A new framework to deal with frame partition problems in computer vision, J Vis Commun Image Represent 13 (2002) 249–268.

[24] Y. Zheng, K. Chen, A hierarchical algorithm for multiphase texture image segmentation, ISRN Signal Process 2012 (2012) 1–11.

[25] J. F. Aujol, G. Aubert, L. Blanc-Feraud, Wavelet-based level set evolution for classification of textured images, IEEE Trans Image Process 12 (2003) 1634–1641.

[26] W. Wei, Y. Xin, A modified multiphase level set evolution scheme for aerial image segmentation, Int J Pattern Recogn 21 (2007) 1195–1212.

[27] M. S. M. D. Abramoff, M. K. Garvin, Retinal imaging and image analysis, IEEE Trans Med Imaging 3 (2010) 169–208.

[28] W. Drexler, J. G. Fujimoto, Optical coherence tomography: Technology and applications, Springer, 2008.

[29] M. Gabriele, G. Wollstein, H. Ishikawa, J. Xu, J. Kim, L. Kagemann, L. Folio, J. Schuman, Three dimensional optical coherence tomography imaging: Advantages and advances, Prog Retin Eye Res 29 (2010) 556–79.

[30] X. Bresson, S. Esedoglu, P. Vandergheynst, J.-P. Thiran, S. Osher, Fast global minimization of the active contour/snake model, J Math Imaging Vis 28 (2007) 151–167.

[31] L. Meziou, A. Histace, F. Precioso, Alpha-divergence maximization for active contour based image segmentation with non-parametric PDF estimations, in: Proc IEEE ICASSP-2012, 2012, pp. 861–864.

[32] E. Parzen, On estimation of a probability density function and mode, Ann Math Statist 33 (1962) 1065–1076.

[33] A. Herbulot, S. Jehan-Besson, S. Duffner, M. Barlaud, G. Aubert, Segmentation of vectorial image features using shape gradients and information measures, J Math Imaging Vis 25 (2006) 365–386.

[34] G. Peyré, J. Fadili, J. Rabin, Wasserstein active contours, in: Proc ICIP-2012, 2012. URL: `http://hal.archives-ouvertes.fr/hal-00593424/`.

[35] W. Crum, O. Camara, D. Hill, Generalized overlap measures for evaluation and validation in medical image analysis, IEEE Trans Med Imaging 25 (2006) 1451–1461.

[36] A. Zijdenbos, B. Dawant, R. Margolin, A. Palmer, Morphometric analysis of white matter lesions in MR images: Method and validation, IEEE Trans Med Imaging 13 (1994) 716–724.

[37] S. Dithmar, F. Holz, Fluorescence Angiography in Ophthalmology, 1 ed., Springer, 2008.

[38] E. Trucco, C. R. Buchanan, T. Aslam, B. Dhillon, Contextual detection of ischemic regions in ultra-wide-field-of-view retinal fluorescein angiograms, in: Proc IEEE EMBC-2007, 2007, pp. 6739–6742.

[39] J. Sivaswamy, A. Agarwal, M. Chawla, A. Rani, T. Das, Extraction of capillary non-perfusion from fundus fluorescein angiogram, in: Proc BIOSTEC-2008, 2008, pp. 176–188.

[40] A. M. Bagci, M. Shahidi, R. Ansari, M. Blair, N. P. Blair, Z. R, Thickness profiles of retinal layers by optical coherence tomography image segmentation, Am J Ophthalmol 146 (2008) 679–687.

[41] I. Ghorbel, F. Rossant, I. Bloch, M. Pques, Modeling a parallelism constraint in active contours. application to the segmentation of eye vessels and retinal layers, in: Proc IEEE ICIP-2011, Brussels, Belgium, 2011, pp. 453–456.